Transaction F: Nanotechnology
Vol. 17, No. 2, pp. 133–147

A Comprehensive Micro-Nanomechanical Drift Modeling and Compensation for Nanorobots

M.H. Korayem[1,*] **and S. Sadeghzadeh**[1]

Abstract. *This paper introduces a new approach for complete drift modeling and compensation for Scanning Probe Microscopes (SPMs) as conventional nanorobots. Although, before this, drift was described as remained error after hysteresis and creep compensation, it can seriously affect SPM performance. Since experimental work accentuated that thermal strain has a dominant contribution, the present model includes only thermal effects. As a significant contribution, an analytical relationship is introduced for heat generation in piezotubes. Then, based on classic heat transfer, the thermal drift for the piezoscanner and microcantilever is modeled. As sub-micro (nano) parts for tip and interfaces in nanoimaging and nanomanipulation modes, the thermal circuit is introduced. Finally, the transfer functions of thermal drift versus ambient temperature variations and piezoscanner heat generation are derived. In this paper, it is not assumed that drift velocity is constant, whereas this assumption was a major drawback of previously presented procedures. This paper, by introducing a comprehensive model and an approximated analytical model, and comparing existent experimental results, shows that the present model is effective and mathematically traceable in both modes.*

Keywords: *Nanorobots; Atomic Force Microscope (AFM); Piezotube; Drift; Micro-nano mechanical modeling.*

INTRODUCTION

Recently, nanorobotic application of nanostructures has gained wide interest for its possible usefulness in chemistry, physics, electronics and medical research. As a new activity for nanorobotic groups, nanomanipulation with nanoscanning devices, especially with AFM, a new horizon has opened in composition, decomposition, assembling, severance and other operations in building and retouching new matters. The AFM has not any comparable rival in nanomanipulation and nanoimaging. However, during any of these operations, undesirable factors hamper the manipulation processes. These undesirable factors may be seen as an increase or decrease in deflections, a necessity for a long period of operation and, in some cases, even failing in operations. Two factors are involved in the fundamental reason for these signs and others; the first is scanner nonlinearities, such as undesirable vibrations, creep behavior and hysteretic loops. These nonlinearities are discussed and compensated with several approaches, such as the new and effective approach introduced by the authors [1]. The second one is ambient effects, which may include variations in ambient conditions, such as temperature, humidity existence and chemical properties, like the PH of ambient. Furthermore, internal error sources, such as heat generation in system components, can also be classified as other ambient effects. In many papers, the remaining error after creep and hysteresis compensation is named 'drift'. However, it is important that in all the literature, without any exception, it is said that drift is a thermal effect rather than anything else [2-6].

In the last decade, several authors have reported experimental approaches for drift compensation [2-6]. These works have three drawbacks: constant velocity assumption for drift behavior, drift compensation in one direction, and lack of theoretical discussion. A short survey of past research can clarify these drawbacks.

Marinellol et al. presented the implementation and validation of a method for accurate imaging of three-dimensional surface topographies [7]. The method provided a correction for the vertical drift.

1. *Robotic Research Laboratory, College of Mechanical Engineering, Iran University of Science and Technology, Tehran, P.O. Box 18846, Iran.*
*. *Corresponding author. Hkorayem@iust.ac.ir*

Received 23 June 2010; received in revised form 17 September 2010; accepted 23 October 2010

Tranvouez et al. applied a drift compensation technique to the AFM manipulation of CdSe colloidal nanorods lying horizontally on a highly oriented pyrolytic graphite surface [8]. Kindt et al. presented a method of eliminating the drift component by sensing and correcting it in real time [9]. Yang et al. introduced a novel automatic compensation scheme to measure and estimate the drift one-step ahead [10]. Lapshin suggested an experimentally proved method for the automatic correction of drift-distorted surface topography obtained with a Scanning Probe Microscope (SPM) [11].

The major drawback of these procedures is their failure to adapt to those situations where the drift velocity changes [4]. They are applicable to correcting images taken over a period of time of approximately constant drift, but cannot support a sequence of nanomanipulation operations that require real-time compensation over a relatively long duration.

According to a general verification, the behavior of the drift depends on factors, such as temperature, humidity, instrument construction procedure, thermal expansion coefficients and chemical characteristics. In this classification, electronic and supply error sources are ignored. Necessarily, for precise applications, such as nanomanipulation, the drift effect should be compensated. However, prior to this, a complete model should be introduced. For a comprehensive model, a typical AFM is considered. Nonetheless, since all SPMs are similar to the considered configuration, the resulted model and compensation scheme are applicable to other SPM configurations. The considered system is depicted in Figure 1. As mentioned in comparable standard experimental work [4-6], we assumed that the substrate is placed at the top of the XY scanner. For a typical device collection, results of this paper are compared with experimental results introduced in [4-6]. The given system is the same as the one implemented on AutoProbe CP-R AFM [5]. Recently, some works were introduced that focused on the real time implementation of drift compensation [12]. They developed an algorithm based on the spatial and temporal correlation of the multiple channel data to derive the pattern position with sub-pixel resolution in real time. Wang et al. applied a local scan strategy to identify the thermal drift contamination in the AFM image [13,14]. Although their strategy reduces the manipulation and imaging time (in a limited range), still online compensation has been achieved. The online compensation needs a micro-nano mechanical model that comprehensively models the mechanical and electrical parts, from nano to macro scale. Recently, Scanning Thermal Microscopes (SThMs) have been introduced that allow the spatial resolution to be improved to 30-50 nm, which allows one to study thermal transport phenomena at these length scales [15]. Therefore, the above mentioned dimensions for measuring thermal characteristics can be accessed using SThM.

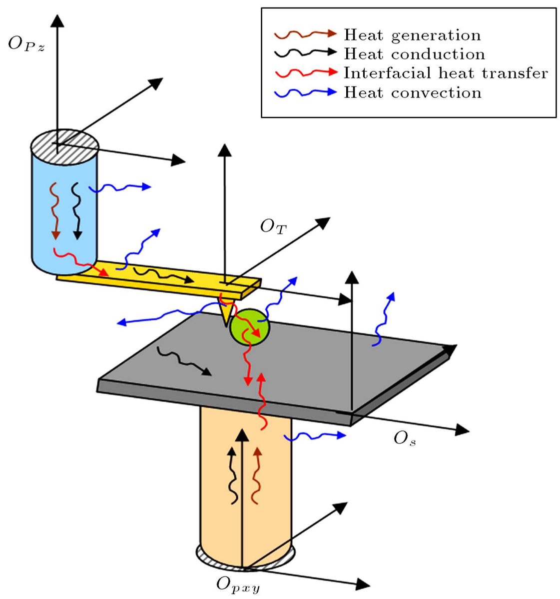

Figure 1. A common configuration for an AFM with nanomanipulation ability and heat transfer mechanism in nanomanipulation scheme.

Schematic of System Configuration and Drift Classification

Figure 1 shows a common configuration for an atomic force microscope with nanomanipulation ability. The upper piezotube is a Z scanner and the one underneath is the XY scanner. The nanomanipulation scheme is achieved by fixing the Z scanner and moving the XY scanner counter to the desired direction. Based on the nonlinearity modeling and compensation scheme introduced in [1], using the current paper, drift calculation and compensation can be added to the hysteresis and creep model. Then, comprehensive nonlinearities modeling, and compensation will be available. In the present configuration, four coordinates exist that are attached to specific points rigidly. Thermal drift can be calculated as the displacement difference between the coordinates. These four frames are:

$$O_{pz}(x_{pz}, y_{pz}, z_{pz}), \qquad O_T(x_T, y_T, z_T),$$

$$O_s(x_s, y_s, z_s), \qquad O_{pxy}(x_{pxy}, y_{pxy}, z_{pxy}),$$

and are named Z scanner, tip, substrate and XY scanner frames, respectively.

Although drift is finalized using a comprehensive model for micro and nano components, a total mechanical model for nano, and an approximate analytical model for micro components, are introduced for comparison and validation.

To facilitate the comparisons, some assumptions are applied to the complete analytical solution. A fin theory for the hollow cylinder and rectangular cantilever is considered, and heat generation is applied as the heat source. An Atomic Force Microscope (AFM) is commonly used in the two modes; nanoimaging and nanomanipulation. Both modes have significant drifts. Suppose that AFM is in nanomanipulation mode that also includes the imaging mode components. Here, for full consideration, all sources are classified into two fields: micro and nano. The micro scale field includes parts from the clamped end of the Z scanner to the tip apex, and the second includes parts from the clamped end of the XY scanner to the top surface of the substrate. An overall view of the present analysis is presented in Figure 2. In Figure 2, any part is separated from another by a box, including the steps done for drift calculation. Green dashed lines show the boundary conditions joining the boxes to each other.

DRIFT MODELING

Although heat transfer through the components produces thermal strains that are related to thermal drift, probable heat transfer through the scanners and ambient is larger and more considerable than other components. The nanoimaging heat transfer mechanism can be obtained as a simple case of Figure 1. There are four types of heat transfer here: Heat Generation, Heat Conduction, Interface Heat Transfer and Heat Convection. Since the scanners have non uniform cross sections and, usually, inharmonic inputs, their heat transfer cannot be modeled in a linear manner in a thermal circuit. All four mechanisms are sufficiently known, except Interfacial Heat Transfer (IHT). There are four IHT in the thermal circuit that are related to the piezotube - cantilever, tip apex - particle, particle - substrate and substrate - piezotube interfaces, respectively. The first and last interfaces are viscoelastic adhesive layers.

Piezotube Strain

For simplification in the analytical solution, a Z piezotube is considered, where a specific voltage is applied

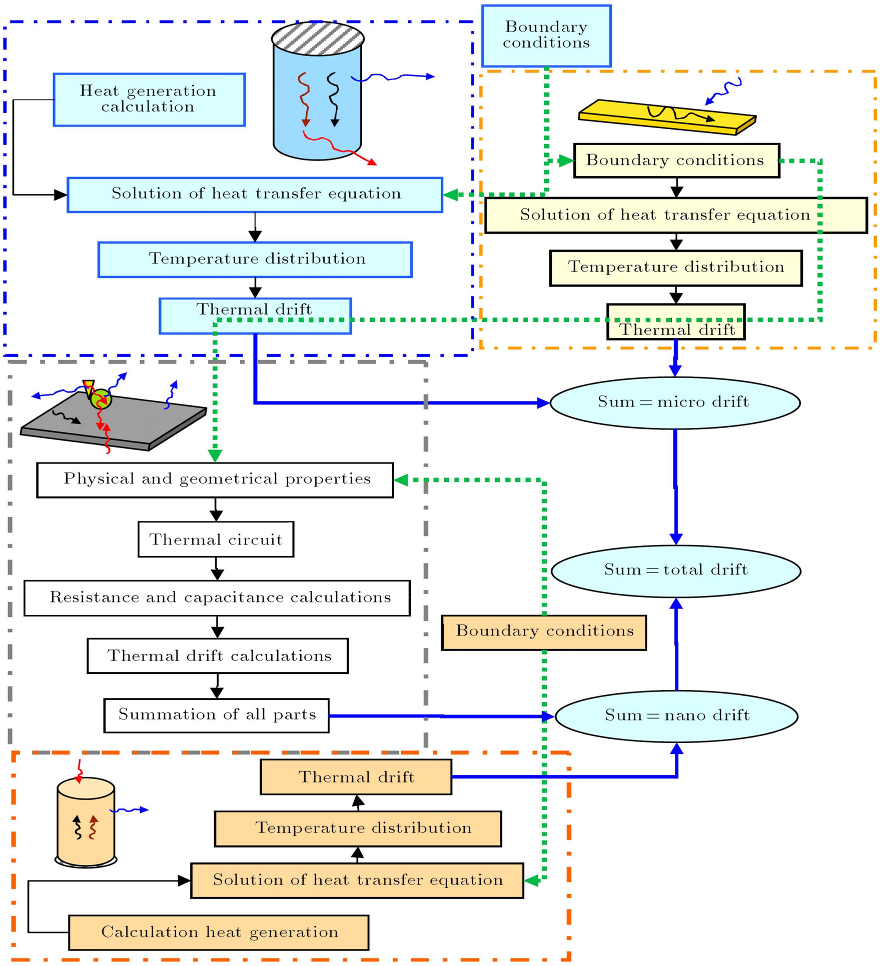

Figure 2. The presented model discipline.

to four quadrants simultaneously, and, therefore, it can be assumed that the piezotube is similar to a stack actuator with equivalent properties. Since base dimensions are bigger than micro and nano components, the actuator base is assumed to have a constant temperature. Mentioned assumptions are applied to the classical fin theory. Equation 1 shows the heat equation and related boundary conditions for the piezotube; assumed in the steady state. As the solution of Equation 1, temperature distribution in the Z scanner can be written as Equation 2:

$$\begin{cases} \frac{d^2T_{pzt}}{dz^2} - \left(\frac{hP}{kA_c}\right)_{pzt}(T_{pzt} - T_{\text{ambient}}) = HG \\ T_{pzt}(z=0) = T_b \\ \left(h(T_{pzt} - T_{amb}) = -k_{pzt}\frac{dT_{pzt}}{dz}\right)\Big|_{z=L_{pzt}} \end{cases} \quad (1)$$

$$T_{pzt}(z) = T_{amb} + m^{-2}\begin{pmatrix} -h+km \\ +e^{2Lm}(h+km) \end{pmatrix}^{-1} \times e^{-mz}\begin{pmatrix} hHG\begin{pmatrix} -e^{Lm} + e^{m(L+2z)} \\ +e^{mz} - e^{m(2L+z)} \end{pmatrix} \\ -km(e^{mz} + e^{m(2L+z)}) \\ -\begin{pmatrix} e^{2mz}(h-km) \\ +e^{2Lm}(h+km) \end{pmatrix} \\ (HG + m^2(T_b - T_{amb})) \end{pmatrix}, \quad (2)$$

where k, m and L are k_p, m_p and L_p, respectively. In addition, $m_p = \sqrt{hP_p/k_pA_{cp}}$ and the parameters h, P_p, k_p and A_{cp} are the coefficient of convection heat transfer, the fin perimeter, the coefficient of conduction heat transfer and the cross section of the area. Also, z, T_b, T_{pzt}, HG and L_p are longitudinal variable, base temperature, temperature in position 'z', heat generated in the piezotube and fin length, respectively. If α_{pzt} be the thermal expansion coefficient, the thermal strain can be calculated as:

$$TS_{\text{piezotube}} = \int_0^L \alpha_{pzt}T_{pzt}(z)dz. \quad (3)$$

Thermal Behavior of Piezoelectric Ceramic Actuators

Piezoelectric ceramics have been extensively used as actuators in intelligent material systems. However, these piezoceramic actuators have their own drawbacks, such as hysteresis [1], creep, small strokes [16] and thermal drift. The heat-dissipation problem associated withpiezoelectric ceramic materials is addressed by [17].

Input voltage produces significant thermal energy that is usually considerable in the length of time needed for several continuous imagings or manipulations. The tip apex and particle position will be affected by the transmission of this heat via cantilever and interfaces. Here, additional displacements that are produced by TC are named *drift*. For pure Z-axis displacement, assuming that every transverse cross section of the tube must remain planar, mechanical strain and stress are as:

$$\varepsilon_z = \frac{d_{31pz}V_{pz}}{2t_{pz}},$$

$$\sigma_z = \frac{d_{31pz}V_{pz}E_{pz}}{2t_{pz}}, \quad (4)$$

where d_{31pz} is the piezoelectric coefficient, V_{pz} is the applied voltage into the Z-piezotube, L_{pz} is the tube length and t_{pz} is the wall thickness of the Z-piezotube. The induced charge on the four quadrant electrodes can be expressed as:

$$Q_i = P_iA = \left[e_{31pz}\left(\frac{e_{31pz}E_tV}{2t}\right)\right]\left[4.\frac{\pi D_t}{4}L_{pz}\right]$$

$$= \frac{e_{31pz}^2\pi D_tL_{pz}E_{pz}}{2t}V_{pz}, \quad (5)$$

where P_i, e_{31pz}, A, E_t, $D_t = (d_{\text{out}}^2 - d_{\text{in}}^2)$, d_{out} and d_{in} are the induced polarization, the piezoelectric charge constant, the area of electrodes, the piezoceramic module of elasticity, the diameter parameter and the outer and inner diameters of a piezotube. Connecting quadrants to the ground, a current will be created as:

$$I_{pz} = \frac{dQ_i}{dt} = \frac{e_{31pz}^2\pi D_tL_{pz}E_{pz}}{2t}\dot{V} = S_i\dot{V}. \quad (6)$$

Then, the dissipative energy is as:

$$DE = V_{pz}I_{pz} = V_{pz}S_i\dot{V} = \frac{e_{31pz}^2\pi D_tL_{pz}E_{pz}}{2t}V_{pz}\dot{V}_{pz}$$

$$= S_{DE}V_{pz}\dot{V}_{pz}. \quad (7)$$

Using the mechanical strain energy created by the input voltage, the energy equilibrium relation leads to the following equation for Heat Generation (HG) in the scanner:

$$\text{HG} = S_{DE}V_{pz}\dot{V}_{pz} - S_{EE}V_{pz}^2, \quad (8)$$

where:

$$S_{EE} = \frac{\pi}{32}E_{pz}D_tL_{pz}\left(\frac{d_{31pz}}{t_{pz}}\right)^2 \quad (\text{N.m/volt}^2),$$

$$S_{DE} = \frac{g_{31pz}^2 \pi D_t L_{pz} E_{pz}}{2t}. \tag{9}$$

For the present system, the parameters lead to 3.77×10^{-11} joules for 1 volt as the piezotubea input. Equation 8 is different from that pointed out in [18].

$$P_{dis} = \tan\delta C V_{0pzt}^2 \omega, \tag{10}$$

where $\tan\delta$ is the dissipation factor, which in common piezo actuators is 5-10% of the total power, and ω is the repetition rate. For a harmonic input as $\sin(10\,t)$, Figure 3 shows a comparison of Equation 8 with Equation 10.

Micro-Cantilever and Tip Drift

Since the micro-cantilever is assumed as a rectangular form importing to the heat transfer mechanism of the scanner, it can be modeled as a rectangular uniform plate. Cantilever base dimensions (Z-piezotube) are bigger than the cantilever, thus, the cantilever base is assumed to have a specific heat flux, generated from the Z-piezotube. These assumptions are applied to the classical fin theory. Equation 11a shows the heat equation and related boundary conditions for the cantilever, assumed in the steady state. As the solution of Equation 11a, temperature distribution in the cantilever can be written as Equation 11b:

$$\begin{cases} \frac{d^2 T_{\text{cant}}}{dx^2} - \left(\frac{hP}{kA_c}\right)_{\text{cant}} (T_{\text{cant}} - T_{amb}) = 0 \\ k_{\text{cant}} \left.\frac{dT_{\text{cant}}}{dz}\right|_{z=0} = k_{\text{piezotube}} \left.\frac{dT_{\text{piezotube}}}{dz}\right|_{x=L} \\ h(T_{\text{cant}} - T_{amb}) = -k_{\text{cant}} \left.\frac{dT_{\text{cant}}}{dx}\right|_{x=L} \end{cases} \tag{11a}$$

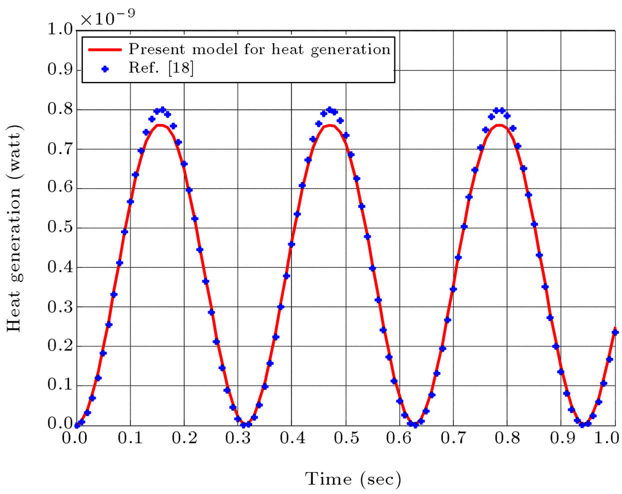

Figure 3. Variation of Heat Generation (HG) in Z-piezotube versus time.

$$T_c(x) = T_{amb}$$

$$e^{-m_c x} h k_p \begin{pmatrix} e^{2m_c x}(k_c m_c - h) \\ +e^{2L_c m_c}(h + k_c m_c) \end{pmatrix},$$

$$+ \frac{\begin{pmatrix} -2e^{L_p m_p} m_p^2 T_b \\ +(e^{L_p m_p} - 1)^2 HG \end{pmatrix}}{k_c m_c m_p \begin{pmatrix} (1 + e^{2L_c m_c})h \\ +(-1 + e^{2L_c m_c}) k_c m_c \end{pmatrix} \begin{pmatrix} (-1 + e^{2L_p m_p})h \\ +(1 + e^{2L_p m_p}) k_p m_p \end{pmatrix}}, \tag{11b}$$

where $m_c = \sqrt{hP_c/k_c A_{cc}}$ that P_c, k_c and A_{cc} are fin parameter, coefficient of conduction heat transfer and cross section area of cantilever, respectively. Also, x, T_c, and L_c are longitudinal variable, temperature in position 'x', and fin length, respectively. If α_c be the thermal expansion coefficient, the thermal strain can be calculated as:

$$TS_{\text{cantilever}} = \int_0^{L_c} \alpha_c T_c(x) dx. \tag{12}$$

Also, the thermal drift of a tip can be calculated using its thermal resistance, and importing to the nano field, as explained later.

ANSYS Modeling for Micro Field

Finite element modeling is used to perform transient thermal analysis. The analysis has been carried out on a rectangular beam (cantilever (thickness = 2 μm, length = 240 μm, width = 8 μm)) supported at the head with the Z scanner. The analysis has been carried out using ANSYS, with element SOLID226 for the piezotube, which has useful capabilities, such as: structural-thermal, piezoresistive, electroelastic, piezoelectric, thermal-electric, structural-thermoelectric and thermal-piezoelectric. For the micro cantilever, element SOLID98 (Tetrahedral Coupled-Field Solid) is used. Simulation calculates the deflection produced by the internal and environmental thermal effects (Figures 4b and 4d). The internal effect is the heat generated from the input voltage of the piezotube (pale black lines in Figure 4b), and the environmental effect is the convection heat transfer (Figures 4b and 4d). These analyses are performed separately. First, the Z scanner model is run and then the temperatures of the cantilever base points on the bottom of the Z scanner are imported to other analyses containing the cantilever

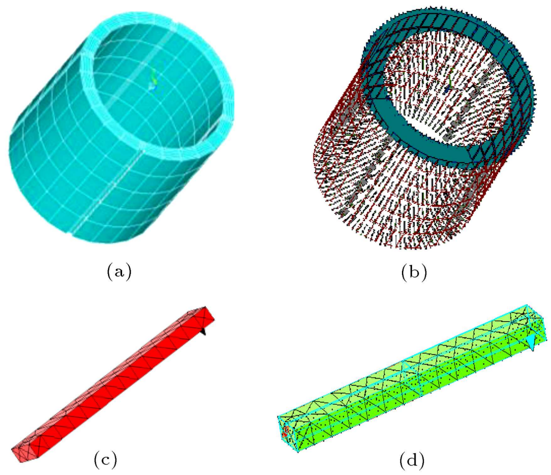

Figure 4. ANSYS modeling for micro parts. (a) The mesh plot of Z scanner; (b) heat sources and boundary conditions for Z scanner; (c) the mesh plot of cantilever; (d) boundary conditions for cantilever.

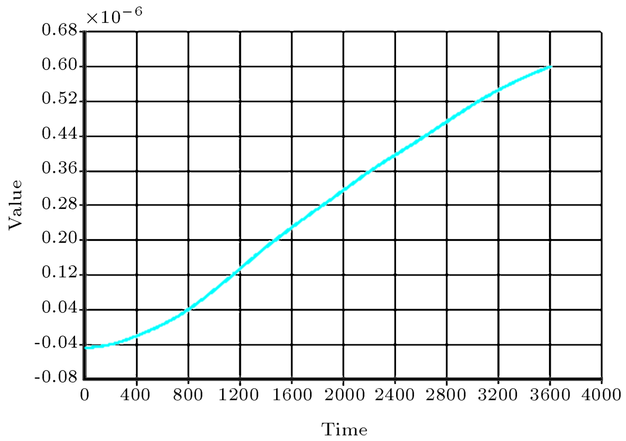

Figure 5. ANSYS results for drift in z direction of end point of cantilever versus time.

model. Finally, the thermal strain of the end point of the cantilever plotted versus time is the final result. Figure 5 shows the drift in the z direction.

The general manipulation schemes have durations of about one hour. The simulated model is based on common manipulation. Other than the fact that drift exists, Figure 5 shows that drift velocity is not linear. Furthermore, in comparison with experimental work, at the end, dominant drift is shown to emanate from piezo scanners.

COMPREHENSIVE MODEL FOR NANO FIELD

Fundamentally, thermal energy can be transferred between contacting bodies by three different modes: conduction at the micro or nano contacts, conduction through the interstitial fluid in the gap between the contacting solids and thermal radiation across the gaps. The radiation heat transfer remains small, less than two percent of the conduction through the micro-contacts, in the range of interest, i.e. $Tc \leq 30^{\circ}$C [19]. Therefore, it can also be neglected here, as for most engineering applications. Thus, the remaining heat transfer mode is only the conduction at the micro and nano contacts.

Thermal Circuit for Nano Field

After introducing the description of heat generation in piezotubes, a complete model for the thermal circuit of imaging and manipulation can now be explained. Here, a comprehensive model is developed that closely matches finite difference simulations. The difference in temperature at interfaces depends on the relative size of thermal resistance within the sides of the interface, as shown in Figure 6. The tip-substrate system includes thermal resistance for the tip, tip-substrate interface, and the substrate itself. Note that heat convection to the air is neglected.

Thermal spreading resistance is defined as the difference between the average temperature of the contact area and the average temperature of the heat sink, which is located far from the contact area, divided by the total heat flow rate, Q ($R = \Delta T/Q$).

Some work in estimating temperature increase at the tip-substrate interface for heated cantilevers is presented, such as the considerable work in [20]. Since high temperature levels have different behavior from low temperature levels, these works are not useful for temperature estimation here. For introducing a comprehensive model, the first step is the resistance formulation.

Formulation of Resistances

- R_{tip}: Since, in semiconductors, the phonon is the dominant heat carrier, using the thermal conductivity of phonons [21], the thermal conduction resistance of the conical portion of the tip can be calculated as:

$$R_{\mathrm{tip}} = \int_{x_1}^{x_2} \frac{dx}{k(x)A(x)} = \frac{LCv(2D_1^2(D_2 - D_1) + \Lambda_0(D_2^2 - D_1^2))}{\Lambda_0 D_1^4(D_1 + D_2)}, \quad (13)$$

where $k(x)$ is the geometry-dependent thermal conductivity, and D_1, D_2, x_1 and x_2 are small diameter, large diameter, distance of tip apex and tip base from the apex of the complete cone, respectively, and $A(x)$ is the cross-sectional area. In addition, C is the volumetric heat capacity, ν is the average

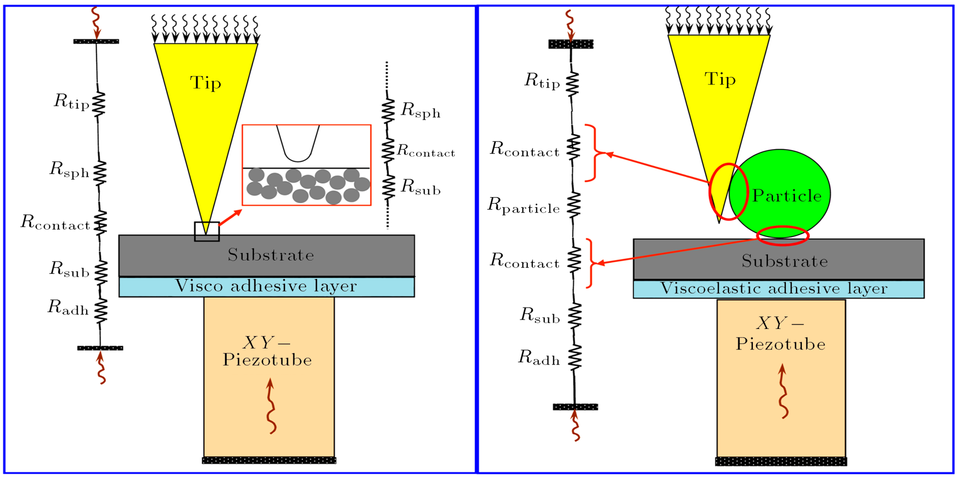

Figure 6. Thermal circuit for heat transfer through the nano field drift in nanoimaging (left) and nanomanipulation (right) modes.

phonon speed, Λ_0 is the temperature-dependent phonon mean free path in bulk material, d is the diameter of the structure, and the effective phonon means that the free path was estimated using Matthiessen's rule [20]. Cv is $\sim 1.8\times 10^9$ W/m°K and Λ_0 is ~ 260 nm for bulk silicon at room temperature [20]. Note that, since the thermal resistance to conduction across the tip cross-section is much smaller than that of outside the tip to the ambient medium, the assumption of one-dimensional heat flow along the axis of the tip in Equation 13 is valid.

- $R_{\rm sph}$: Since the arbitrary tip apex geometry produces a thermal resistance, a separate resistance is required for the hemispherical cap at the apex of the tip to account for its geometry; $R_{\rm sph}$ is equal to [20]:

$$R_{\rm sph}=\frac{1}{k_{\rm sph}\pi r}\tanh^{-1}\left(1-\frac{1}{2}cLn\left(\frac{1+c}{1-c}\right)\right), \tag{14}$$

where $k_{\rm sph}$ is the thermal conductivity of the hemispherical cap and c is determined by Equation 15:

$$F=\frac{G_{sub}r}{1-\eta}\left[(c^2+1).Ln\left(\frac{1+c}{1-c}\right)-c\right], \tag{15}$$

where F is the contact force, G_{sub} is the shear modulus of the substrate, and η is Poisson's ratio for the substrate [20].

- $R_{\rm contact}$: A large thermal resistance may exist due to imperfect contact, for example, surface roughness. Generally, the value of contact resistance depends on surface conditions, the adjacent difference across the interface, materials and contact pressure. On the other hand, the material is important because, even with a perfect contact, thermal resistance exists between dissimilar materials due to the acoustic mismatch, which is especially considerable at low temperatures. The interfacial resistance is as [22]:

$$R_{\rm contact}=\frac{4R_b}{\pi a^2}, \tag{16}$$

where R_b is the thermal boundary resistance and has the same units as the bulk thermal contact resistance [22]. In experiments, for solid-solid contacts close to room temperature, R_b does not vary seriously with the contacting materials and is usually about 5×10^{-9} to 5×10^{-7} m^{2}K/W [23]. For tip penetration into a soft substrate, and nanomanipulation conditions, the effective contact diameter can be estimated as [20]:

$$a=\sqrt{8rb}, \tag{17}$$

where b is the penetration depth of the tip into a soft substrate.

- R_a: When the film thickness becomes comparable to, or smaller than, the phonon mean free path, the size and interface effects become significant, and the Boltzmann transport equation should be applied to describe phonon transport. Although all previous studies have largely focused on planar thin films, a wide range of micro and nano-scale thermal problems are associated with nonplanar geometries, such as spherical and cylindrical media, which have not been studied completely [24]. Here, considering a nanometer scale medium with spherical geometry, the thermal resistance of the medium is derived. Consider a concentric spherical nano media shell with inner and outer radius, r_1 and r_2, respectively. The heat flux on the shell can be written as [24]:

$$Q_{\rm sphere}=\frac{\frac{1}{3}Cv\Lambda(T_1-T_2).(3\pi r_1^2/\Lambda)}{\begin{pmatrix}(1-(\tau'_{21}+\tau'_{12})/2)/\tau''_{21}\\ +(1-(\tau'_{23}+\tau'_{32})/2)r_1^2/(\tau''_{23}r_2^2)\\ +3\Lambda r_1(1-(r_1/r_2))/4\end{pmatrix}}, \tag{18}$$

where $Q_{\text{sphere}} = 4\pi r^2 q(r)$ is the total heat flux and:

$$\tau'_{21} = \frac{3}{2\pi}\int_0^{\pi} \tau_{21}\sin\theta\cos\phi d\Omega_r, \tag{19a}$$

$$\tau'_{12} = \frac{3}{2\pi}\int_0^{\pi} \tau_{12}\sin\theta\cos\phi d\Omega_r, \tag{19b}$$

$$\tau''_{21} = \frac{1}{\pi}\int_0^{\pi} \tau_{12} d\Omega_r, \tag{19c}$$

where Λ, τ_{ij}, Ω_r, θ, ϕ are the phonon average mean free path, the transitivity, the solid angle in the r direction, the polar angle and the azimuthal angle, respectively. Since, here, the interfaces are assumed to be totally diffusing, the transitivity is [24]:

$$\tau_{ij} = \frac{C_j v_j}{C_i v_i + C_j v_j}. \tag{20}$$

For modeling heat transfer in the complete nanoparticle, it is assumed that the nanoparticle is formed from a number of concentric spherical nano media. Hence by applying the thermal resistance relation, the partial thermal resistance that is the thermal resistance of the considered shell should be as:

$$R_a = \frac{T(r) - T(r_1)}{Q} = \frac{\left[1 - \frac{\tau'_{21}+\tau'_{12}}{2}\right]}{\pi C v r_1^2 \tau''_{21}} + \frac{\left[1 - \frac{\tau'_{23}+\tau'_{32}}{2}\right]}{\pi C v r_2^2 \tau''_{23}} + \frac{3}{4\pi C v r_1}\Lambda\left[1 - \frac{r_1}{r_2}\right]. \tag{21}$$

Now, for total thermal resistance from the tip-particle interface to the particle-substrate interface, the series configuration can be dealt with:

$$R_a = \sum_{i=1}^{n}\left[\frac{\left[1 - \frac{\tau'_{21}+\tau'_{12}}{2}\right]}{\pi C v r_{1i}^2 \tau''_{21}} + \frac{\left[1 - \frac{\tau'_{23}+\tau'_{32}}{2}\right]}{\pi C v r_{2i}^2 \tau''_{23}} + \frac{3\Lambda\left[1 - \frac{r_{1i}}{r_{2i}}\right]}{4\pi C v r_{1i}}\right]. \tag{22}$$

It is obvious that the phonon path is not specific, whereas Equation 22 gives outer surface to particle centre resistance. Hence, a statistical analysis is needed. Assume that the two contact points be identified by two contact zones, A_1 and A_2. Since contact angles in the nanomanipulation scheme are specific, for general configuration, Figure 7b shows the contact parameters. The lower contact area,

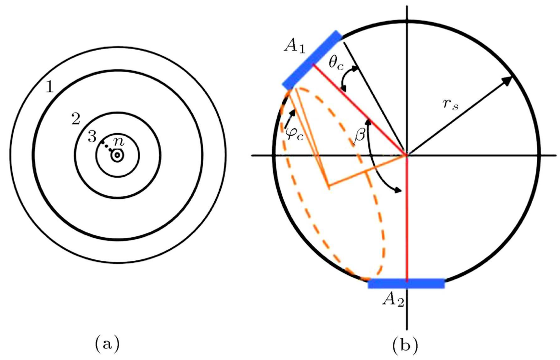

Figure 7. (a) The nanoparticle is formed from some number of concentric spherical nano media. (b) The nanoparticle contacts parameters.

A_2, is fixed because the particle-substrate contact is always in a horizontal direction. Nonetheless, upper contact area, A_1, can be moved for different contact angles. The dashed circle is the contact circle, and φ_c is the contact angle in the contact circle.

The partial differential equation and the related conditions for this problem description will be as:

$$\frac{\partial T}{\partial t} = \alpha\left[\frac{\partial^2 T}{\partial r^2} + \frac{2}{r}\frac{\partial T}{\partial r} + \frac{1}{r^2\sin^2\theta}\frac{\partial^2 T}{\partial \varphi^2} + \frac{1}{r^2\sin\theta}\frac{\partial}{\partial\theta}\left(\sin\theta\frac{\partial T}{\partial\theta}\right)\right]$$

$$\begin{cases} \begin{cases} -k\frac{\partial T}{\partial r} = Q, \begin{cases} r = r_s \\ (\beta-\theta_c)/2 < \theta < (\beta+\theta_c)/2 \\ 0 < \varphi < \varphi_c \end{cases} \\ -k\frac{\partial T}{\partial r} = -Q \\ \begin{cases} r = r_s \\ (\beta-\theta_c)/2 < \theta < (\beta+\theta_c)/2 \\ 0 < \varphi < (\pi+\varphi_c) \end{cases} \\ -k\frac{\partial T}{\partial r} = h_{amb}(T_{r=r_s} - T_{\text{ambient}}) \\ \begin{cases} r = r_s \\ (\beta-\theta_c)/2 > \theta \text{ or } \theta > (\beta+\theta_c)/2 \\ \varphi_c < \varphi < \pi \text{ or } (\pi+\varphi_c) < \varphi < 2\pi \end{cases} \end{cases} \end{cases} \tag{23}$$

The quantity of h_{amb} is very small versus the conduction effect, because the ambient gases have a bigger free path than bulk solids, such as silicon. We assume that, as in experimental work, the nanoparticle is a gold particle. Since convection heat transfer in the ambient - nanoparticle effect is very small, the third condition will be approximated as:

$$\left(-k\frac{\partial T}{\partial r}=0\right).$$

- R_{sub}: Here, heat transfer through the substrate is approximated as a circular heat source in contact with a flat, semi infinite substrate. The ratio of the thermal resistance of a substrate of finite thickness (R_{sub}) to that of a semi infinite case will come as [22]:

$$R_{sub}=\int_0^\infty\int_0^\infty \frac{2\sin\alpha\sin\beta\tanh\left(\frac{2t_{sub}}{a\sqrt{\pi}}\sqrt{\alpha^2+\beta^2}\right)}{k_{sub,o}a\pi^{5/2}\sqrt{\alpha^2+\beta^2}}d\alpha d\beta, \quad (24)$$

where $k_{sub,o}$ is the bulk substrate thermal conductivity and t_{sub} is the substrate film thickness.

DRIFT ESTIMATION AND IDENTIFICATION

Using a MATLAB code and validating with an ANSYS package, the transfer function of drift behavior is derived. Since, for transfer function analysis (dynamic behavior), the capacitance of components should be considered, Table 1 shows the specific heat capacitance and shape factors of components [25].

Thermal drift sources are the ambient temperature and input voltages in X, Y and Z directions. Although ambient temperature and Z-direction voltage are completely independent of others, the X and Y direction thermal drifts are dependent on each other. Furthermore, the X drift dependency on the Y voltage and the Y drift dependency on the X voltage should be estimated for accurate modeling of their related drift. After importing the results to the system identification toolbox of MATLAB, the transfer functions are achieved (see Appendix).

Since the length of the A_{yQ_x} matrix is equal to the rank of CO_{yQ_x}, the system is controllable. Using the feedback state space design, the poles are placed at points [-1 -1.2 -2]. Then new system is converted to zero-pole-gain models (ZPK objects). The new plant in state space form has a matrix as:

$$A_{yQ_x\text{new}}=A_{yQ_x}-B_{yQ_x}\times K,$$

and the resulted model is as:

$$G_{yQ_x}(s)=\frac{1.3432\times10^{-22}(s^2-2.224s+1.24)}{(s+2)(s+1.2)(s+1)}. \quad (25)$$

For the close loop system, the stability range is:

$$1.37\times10^{16}\le K\le1.63\times10^{22}.$$

Figure 8 shows the block diagram of the closed loop system. The compensator is adopted as $H=1$, $F=1$ and $C=1.37\times10^{16}$. High-gain feedback control is a common method in experimental work to minimize

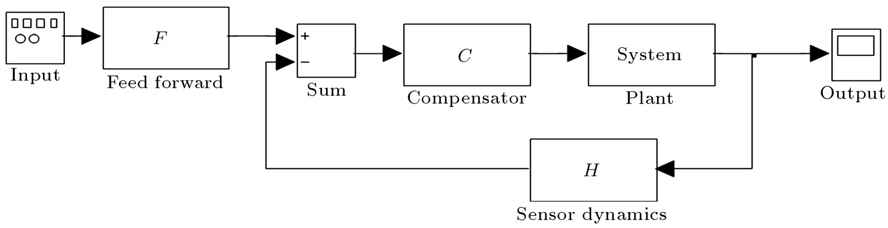

Figure 8. Block diagram of closed loop system.

Table 1. Specific heat capacitance and shape factors of components.

Parts	Material	*C*	Shape	Parameters	Capacitance
Pzt	Pzt 5H	440	Hollow cylinder	$\gamma=0.5''/0.49$	419.32
				$C_f=0.953$	
				Table IV of [25]	
Cantil.	Silicon nitride	710.6	Rectang. cantilever	$C_f=0.928$	659.44
				Table III of [25]	
Tip	Silicon nitride	710.6	Conical	$C_f=0.953$	675.07
				Between 0.953 and 1. [25]	
Particle	Gold	130	Sphere	$C_f=1$ [25]	130
Subst.	Mica	880	Rectang. plate	$C_f=0.928$	816.64
				Table III of [25]	

positioning error caused by drift, hysteresis and creep. This value is theoretical and, in practice, based on the system configuration and properties, it may be smaller. However, this value is the gain of displacement to the heat generated and, so, is in a usual range. For implementation, the voltage amplifiers should be utilized.

Based on steady state heat transfer, and, as thermal resistance and heat passing from interfaces are constant, drift in interfacial fields can be calculated using Equation 26:

$$\mathrm{Drift}_{IHT} = (\alpha \times R)_{\mathrm{interface}} \times q_{\mathrm{pass}}, \tag{26}$$

where α and R are equivalent thermal expansion and thermal resistance along the interface, respectively. Thus, in nanoimaging mode, the total nano drift is as:

$$\mathrm{Drift}_{\text{Nano field in nanoimaging}} = \sum_{i=1}^{4} \alpha_i R_i q_i, \tag{27}$$

where $i = 1, 2, 3, 4$ indicates the tip, sph, contact and glue (adhesive layer), respectively. In the nanomanipulation mode, the total nano drift is as:

$$\mathrm{Drift}_{\text{Nano field in nanomanipulation}} = \sum_{i=1}^{4} \alpha_i R_i q_i, \tag{28}$$

where $i = 1, 2, 3, 4$ indicates the tip, contact1, contact 2 and particle, respectively. The coefficient of thermal expansion of the epoxy is about $70 \times 10^{-6}(1/c)$ [26]. Usually, the thermal resistance of adhesive layers is taken to be about 20×10^{-6} m^{2}K/W [26]. After simulation, the nano thermal drift is calculated in a usual nanomanipulation scheme for a 3600 seconds operation of AFM. Figure 9 shows the result of this simulation.

RESULTS AND DISCUSSION

Comparison

Two comparisons are done for comparison. Firstly, for the nanoimaging process, experimental data from [6] are compared and, then, for the nanomanipulation scheme, simple and automated nanomanipulation works are compared [5]. The first device is "Veeco Dimension 3100", which was tested in the work of Zhikun Zhan et al. [6]. Based on this work, some needed information is applied to the model. Generally, the heat causing the temperature change of the scanner mainly comes from the components contained in an AFM system, because the environmental temperature is controlled strictly. Furthermore, it should be mentioned that room temperature is about (20 ± 2°C). Other information is introduced in Table 2.

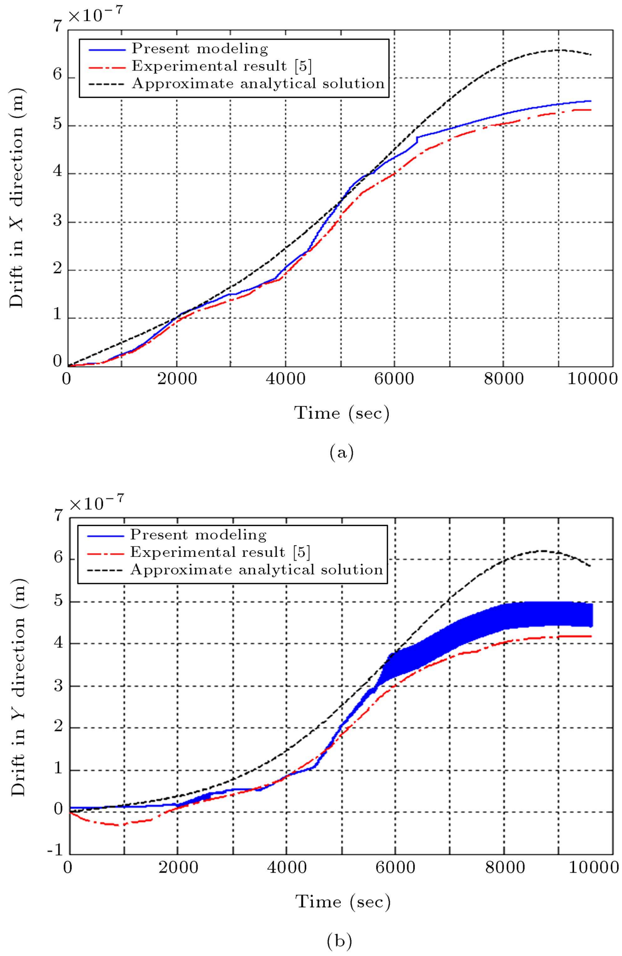

Figure 9. Present modeling and experimental results comparison for X (a) and Y (b) direction for an AutoProbe CP-R AFM [4].

The second device is an AutoProbe CP-R AFM (Park Scientific Instruments). In [4], results were obtained on the AutoProbe AFM with a sharp tip in dynamic mode, imaging and manipulating gold nanoparticles with nominal diameters of 15 nm, deposited on a mica surface, and covered with poly-L-lysine in the air, at room temperature and humidity.

Results show some discrepancy from experimental data. Researchers have speculated that thermal drift is one of the major causes of error for nanomanipulation using AFM systems, but until now, mathematical or mechanical analyses of the AFM drift phenomenon have not been introduced. The best analyses used for drift studies were quantitative, which cannot introduce an acceptable and useful enough view of drift. Since present results are in agreement with experimental data, the idea that thermal drift is one of the major causes of error for nanomanipulation and nanoimaging using AFM is acceptable. This expression was mentioned in many previous papers without any proof. Although the present simulation

Table 2. Data for comparison of "Veeco Dimension 3100", mentioned in [6].

AFM Components and Material	Pzt 5H	Cantilever-Tip (Silicon Nitride)	Grid (Silicon)	Platform (Steel)
Thermal expansion coefficient (1/K)	$1 \sim 5e-6$	3e-6	2.6e-6	1.2e-5
Original length (μm)	40,000	134	10	10
Change in length (nm/K)	$40 \sim 200$	8.4e-2	1.82e-2	28.2e-2

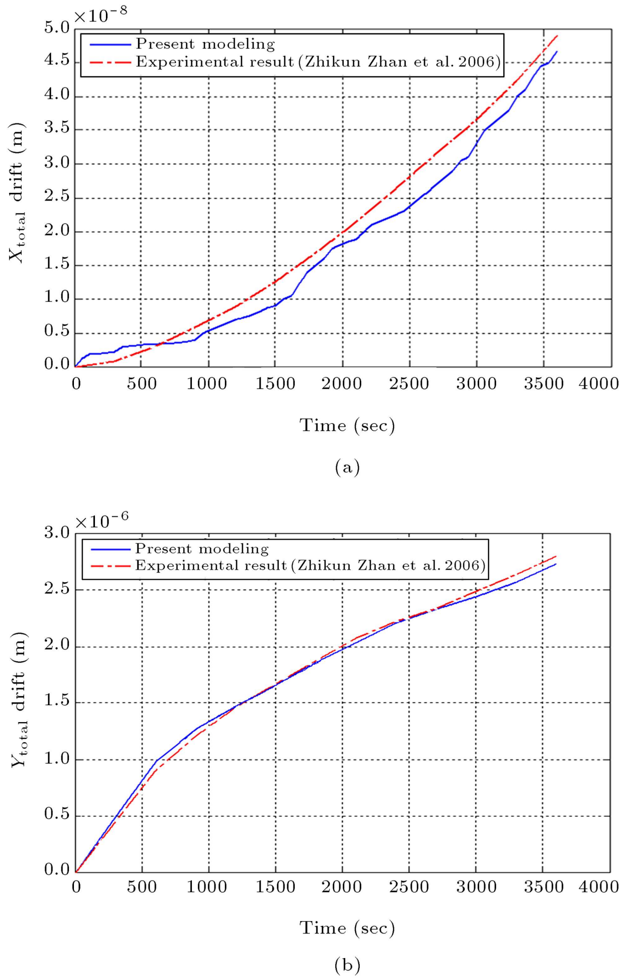

Figure 10. Comparison in X (a) and Y (b) direction for Zhikun Zhan et al. experimental setup [6].

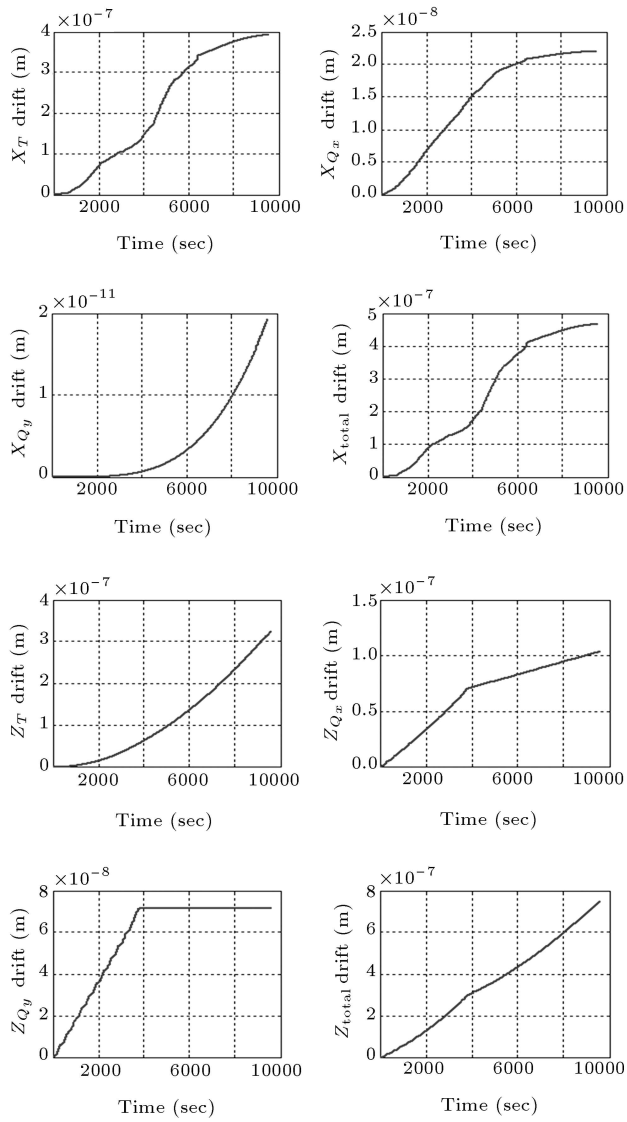

Figure 11. X and Z direction results for all of inputs, from present modeling, for an AutoProbe CP-R AFM [4].

is not totally analytical, an approximate analytical model is introduced here. As Figure 10 shows, the discrepancy in the X direction has increased as time increased. The chatter behavior is from the numerical solution of the system using the simulink. It should be noted that the convergence study had been done, and increasing (limited) or decreasing time steps has not had a considerable effect on the responses. The present modeling is also acceptable among other effects, such as ambient PH, humidity etc. It seems that at room conditions, humidity is more significant than others. Thus for future works, humidity consideration has the highest precedence.

For more details, Figure 11 shows X and Z direction drifts for an AutoProbe CP-R AFM. As Figure 11 shows, effects of ambient temperature are most

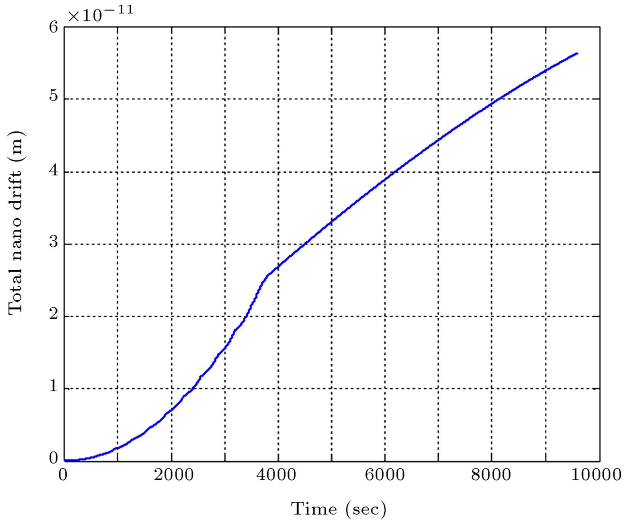

Figure 12. Total nano drift for an AutoProbe CP-R AFM [4].

significant. For drift in the XY plane, the contributions of ambient temperature and heat generation in X and Y directions on the drift are about 100, 10 and 0.01 nanometers, respectively. For the Z direction, these values are 100, 100 and 10 nanometers, respectively. These data are in agreement with experimental works, some of which have been compared in the comparison section. Figure 12 shows the total nano drift for an AutoProbe CP-R AFM. It is observed that drift due to nano fields is in the order of 0.01 nanometers. This drift is much smaller than that of the micro field. This is the most important factor in verifying prior theoretical work.

Error Analysis

In this section, the probable error sources of the modeling and experimental results are investigated and an estimation of measurement errors is derived. The error sources are, in general, different physical characteristics and the misalignment of mechanics.

Errors due to misaligned mechanics include dimensional and relational errors. Although some dimensions may have some discrepancies with the experimental setup, they are not larger than 1/5 for the length ratio. The present model shows that errors for ratios smaller than 1/5, are negligible. Besides, the piezotubes in the considered system and all SPMs are symmetric versus their axis. This property decreases some errors systematically. Nonetheless, some errors can be from mechanical values, such as force relations needed for our estimation of some parameters. In these relations, the misalignment is, in some part, because of our contribution. Thus their accuracy will be discussed at the end.

CONCLUSION

The present paper introduced a comprehensive drift model for AFM nanomanipulation and nanoimaging. Comparisons show that the presented model is effective, simple and mathematically traceable. Furthermore, a related compensation scheme can be applied. For a complete, effective and practical model, all parameters have been considered here. Some macro models have been presented before, but they are not applicable to nano scale components. Thus, new relations, based on nano-scale mechanical properties, are introduced here. Furthermore, an analytical relation is introduced for heat generation in piezotubes. For control management, a transfer function analysis of the system is introduced that is general. Although some transfer functions are in state space form, to simplify the compensation and control scheme, the transfer functions of the drifts are derived in the simplest form. These transfer functions are the ratios between X, Y and Z drifts to the drift sources. The results show that, in general, the temperature variance of the ambient has the dominant effect. Heat generation in the X direction is the next significant effect, and heat generation in the Y direction has the smaller drift in comparison to others. An important and novel property of this paper is the consideration of velocity. As the final figures depict, drift velocity varies truly versus time, and this is a significant difference between this model and others.

The predicted temperature disturbance is near to experimental results, and observed discrepancies could originate from surface pollution and impairments that increase the solid-solid contact area. In any case, some assumptions used here may be different from those under experimental conditions. For example, the mechanical stability of the glue is very important. At several places in the SPMs, glue has been used to connect different parts. There is no alternative to using glue in any of these cases. Although the layers of glue can have some unwanted effects, e.g. hysteresis or creep, thermal drift can be crucial here. The designers can prevent these effects by using thin layers of glue.

NOMENCLATURE

O_{pz}	Z scanner frame
O_T	tip frame
O_s	substrate frame
O_{pxy}	XY scanner frame
h	coefficient of convection heat transfer
P_{pzt}, P_c	scanner and cantilever perimeter
k_{pzt}	coefficient of conduction heat transfer
A_{cp}	cross section of area
z	longitudinal variable

T_b	base temperature
T_{pzt}	temperature in position 'z'
HG	heat generated in piezotube
L_{pzt}	fin length
α_{pzt}	thermal expansion coefficient
d_{31pz}	piezoelectric coefficient
V_{pz}	applied voltage into Z-piezotube
L_{pz}	tube length
t_{pz}	wall thickness of the Z-piezotube
Q_i	induced charge
P_i	induced polarization
e_{31pz}	piezoelectric charge constant
A	area of elecrodes
E_t	piezoceramic module of elasticity
k_c	coefficient of conduction heat transfer
A_{cc}	cross section area of cantilever
x	longitudinal variable
$d_{\text{out}}, d_{\text{in}}$	outer and inner diameter of piezotube
$\tan\delta$	dissipation factor
ω	repetition rate
T_c	temperature in position 'x'
L_c	fin length
α_c	thermal expansion coefficient
R_{tip}	thermal conduction resistance of conical portion of tip
$k(x)$	geometry-dependent thermal conductivity of tip
D_1, D_2	small and large diameter
x_1, x_2	distance of tip apex and tip base from apex of complete cone
$A(x)$	cross-sectional area of tip
C	volumetric heat capacity
v	average phonon speed
Λ_0	temperature-dependent phonon mean free path
d	diameter of structure
R_{sph}	thermal resistance of hemispherical cap at tip apex
k_{sph}	thermal conductivity of hemispherical cap
F	contact force
G_{sub}	shear modulus of substrate
η	Poisson ratio of substrate
R_{contact}	interfacial resistance
R_b	thermal boundary resistance
b	penetration depth
R_a	thermal resistance of particle
Q_{sphere}	heat flux on shell
τ_{ij}	transmissivity
Ω_r	solid angle in r direction
θ, ϕ	polar and azimuthal angles
R_{sub}	thermal resistance of substrate
$k_{sub,o}$	bulk substrate thermal conductivity
t_{sub}	substrate film thickness
G_{IJ}	transfer function of drift in I direction, generated from source J
T	ambient temperature (a drift source)
Q_x	heat of x direction (a drift source)
Q_y	heat of y direction (a drift source)
Q_z	heat of z direction (a drift source)

REFERENCES

1. Korayem, M.H. and Sadeghzadeh, S. "A new modeling and compensation approach for creep and hysteretic loops in nanosteering by SPM's piezotubes", *Int. J. Adv. Manuf. Technol.*, **44**(7-8), pp. 829-840 (2009).

2. Yurov, V.Y. and Klimov, A.N. "Scanning tunneling microscope calibration and reconstruction of real image: drift and slope elimination", *Rev. Sci. Inst.*, **65**(5), pp. 1551-1557 (1994).

3. Staub, R. et al. "Drift elimination in the calibration of scanning probe microscopes", *Rev. Sci. Inst.*, **66**(3), pp. 2513-2516 (1995).

4. Mokaberi, B. and Requicha, A.A.G. "Compensation of scanner creep and hysteresis for AFM nanomanipulation", *IEEE Int. Conf. Robotics and Automation*, **5**(2), Art. No. 4358078, pp. 197-206 (2004).

5. Mokaberi, B. and Requicha, A.A.G. "Drift compensation for automatic nanomanipulation with scanning probe microscopes", *IEEE Transactions on Automation Science and Engineering*, **3**(3), pp. 199-207 (2006).

6. Zhikun, Z. et al. "AFM operating-drift detection and analyses based on automated sequential image processing", *7th IEEE International Conference on Nanotechnology - IEEE-NANO 2007, Proceedings*, Art. No. 4601295, pp. 748-753 (2007).

7. Marinello, F. and Bariani, P. et al. "Fast technique for AFM vertical drift compensation", *Measurement Science and Technology*, **18**(3), pp. 689-696 (2007).

8. Tranvouez, E. et al. "Active drift compensation applied to nanorod manipulation with an atomic force microscope" *Rev. Sci. Instrum.*, **78**, p. 115103 (2007).

9. Kindt, J.H. et al. "Atomic force microscope detector drift compensation by correlation of similar traces acquired at different set points", *Rev. Sci. Instrum.*, **73**, p. 2305 (2002).

10. Yang, Q. et al. "Automatic drift compensation using phase correlation method for nanomanipulation", *IEEE Transactions on Nanotechnology*, **7**(2), pp. 209-216 (2008).

11. Lapshin, R.V. "Automatic drift elimination in probe microscope images based on techniques of counter-scanning and topography feature recognition", *Measurement Science and Technology*, **18**(3), pp. 907-927 (2007).

12. Sergey, B., Jian, S. and Chanmin, S. "AFM image based pattern detection for adaptive drift compensation and positioning at the nanometer scale", *2008 American Control Conference*, ACC, Seattle, WA, Code 73572 (2008).

13. Wang, Y., Li, G., Xi, N. and Liu, L. "Compensation of drift contamination in AFM image by local scan", *Proceedings of the 2008 IEEE International Conference on Robotics and Biomimetics*, Thailand (2008).

14. Wang, Y., Li, G. and Liu, L. "Local scan for compensation of drift contamination in AFM based nanomanipulation", *2009 IEEE/RSJ International Conference on Intelligent Robots and Systems*, IROS (2009).

15. Li, S. et al. "Scanning thermal microscopy of carbon nanotubes using batch-fabricated probes", *Appl. Phys. Lett.*, **77**, p. 4295 (2000).

16. Giurgiutiu, V. et al. "Large-amplitude rotary induced-strain (laris) actuator", *J. Intell. Mater. Syst. Struct.*, **8**, pp. 41-50 (1997).

17. Shahinpoor, M. and Schneider, H.J. "Intelligent materials", *The Royal Society of Chemistry*, Cambridge CB4 0WF, UK, pp. 231-255 (2008).

18. http://www.physikinstrumente.com

19. Bahrami, M. et al. "Modeling of thermal joint resistance of polymer-metal rough interfaces", American Society of Mechanical Engineers, Heat Transfer Division, (Publication) HTD, **375**(2), IMECE2004-60131, pp. 211-220 (2004).

20. Nelson, B.A. and King, W.P. "Modeling and simulation of the interface temperature between a heated silicon tip and a substrate", *Nano-scale and Microscale Thermophysical Engineering*, **12**(1), pp. 98-115 (2008).

21. Ashcroft, N.W. and Mermin, N.D., *Solid State Physics*, Saunders College Publishing-Harcourt Brace College Publishing, Orlando, Florida (1976).

22. Incropera, F.P. and DeWitt, D.P., *Fundamentals of Heat and Mass Transfer*, 5th Ed., Wiley, New York, (2002).

23. Beechem, T. et al. "Role of interface disorder on thermal boundary conductance using a virtual crystal approach", *Appl. Phys. Lett.*, **90**, 054104 (2007).

24. Taofang, Z. and Wei, L. "Phonon heat conduction in micro- and nano-core-shell structures with cylindrical and spherical geometries", *Journal of Applied Physics*, **93**, p. 4163 (2003).

25. Chow, Y.L. and Yovanovich, M.M. "The shape factor of the capacitance of a conductor", *Journal of Applied Physics*, **53**(12), pp. 8470-8475 (1982).

26. Dillard, D.A. and Pocius, A.V. "Adhesion science and engineering-I, the mechanics of adhesion", *Elsevier*, ISBN: 0 444 51 140 7 (2002).

APPENDIX

Importing the results to the System Identification toolbox of MATLAB, the transfer functions are achieved. Here, G_{ij} is the transfer function of drift in direction I, generated from source J.

$$G_{xT}=\frac{K(1+T_z s)\exp(-T_d s)}{(1+T_{p1}s)(1+T_{p2}s)}, \tag{A1}$$

$$G_{yT}=\frac{K(1+T_z s)\exp(-T_d s)}{s(1+T_{p1}s)(1+T_{p2}s)}, \tag{A2}$$

$$G_{zT}=\frac{K(1+T_z s)\exp(-T_d s)}{(1+T_{p1}s)(1+T_{p2}s)}, \tag{A3}$$

$$G_{xQ_x}=\frac{K(1+T_z s)}{(1+T_{p1}s)(1+T_{p2}s)(1+T_{p3}s)}, \tag{A4}$$

$$G_{yQ_x}=\begin{cases}x(t+Ts)=A_{yQ_x}x(t)+B_{yQ_x}u(t)+K_{yQ_x}e(t)\\ y(t)=C_{yQ_x}x(t)+D_{yQ_x}u(t)+e_{yQ_x}(t)\end{cases} \tag{A5}$$

$$G_{zQ_x}=\frac{K(1+T_z s)}{s(1+T_{p1}s)(1+T_{p2}s)(1+T_{p3}s)}, \tag{A6}$$

$$G_{xQ_y}=\frac{K}{s((1+2\zeta T_w)s+(T_w s)^2)}, \tag{A7}$$

$$G_{yQ_y}=\begin{cases}x(t+Ts)=A_{yQ_y}x(t)+B_{yQ_y}u(t)+K_{yQ_y}e(t)\\ y(t)=C_{yQ_y}x(t)+D_{yQ_y}u(t)+e_{yQ_y}(t)\end{cases} \tag{A8}$$

$$G_{zQ_y}=\frac{K(1+T_z s)\exp(-T_d s)}{(1+T_{p1}s)(1+T_{p2}s)(1+T_{p3}s)}, \tag{A9}$$

where, for the considered system, all coefficients are

Table A1. Drift transfer functions coefficients.

Case	K	T_{p1}	T_{p2}	T_{p3}	T_z	T_d
X_T	5.8e-9*	0.001	907.8	–	-6809.4	0
Y_T	7.35e-17	0.001	0.001	–	6335.1	0
Z_T	7.7e-3	84732.9	3.1437	–	6327.3	0
X_{Q_x}	9.075e-11	0.001	213.33	0.001	52.224	–
Y_{Q_x}	–	–	–	–	–	–
Z_{Q_x}	9454e-14	0.001	28544.2	0.001	3182.2	–
X_{Q_y}	7781e-12	$T_w = 0.001$	$\zeta = 16.1e7$	–	–	–
Y_{Q_y}	–	–	–	–	–	–
Z_{Q_y}	8536e-8	0.001	13.05e5	55779	1563066	30

$^*5.8e-9 = 5.8 \times 10^{-9}$

introduced in Table A1, and, also;

$$A_{yQ_x} = \begin{bmatrix} 1.0001 & 0.00063 & 0.00054 \\ 0.0040 & 0.90031 & -0.858 \\ 0.0060 & -0.0823 & -0.465 \end{bmatrix},$$

$$B_{yQ_x} = \begin{bmatrix} 2.26e-10 & -2.65e-7 & -4.52e-7 \end{bmatrix}^T,$$

$$C_{yQ_x} = \begin{bmatrix} 5.25e-13 & -7.62e-17 & 1.06e-17 \end{bmatrix},$$

$$D_{yQ_x} = [0],$$

$$K_{yQ_x} = \begin{bmatrix} 1.82e12 & -1.11e14 & 1.64e13 \end{bmatrix}^T, \tag{A10}$$

$$A_{yQ_y} = \begin{bmatrix} 0.9997 & 0.000295 & 0.00045 \\ 0.0062 & 0.98074 & -0.478 \\ 0.000947 & -0.0083 & -0.355 \end{bmatrix},$$

$$B_{yQ_y} = \begin{bmatrix} 4.61e-8 & -3.88e-5 & -0.00011 \end{bmatrix}^T,$$

$$C_{yQ_y} = \begin{bmatrix} 9.97e-13 & -1.89e-16 & 3.45e-18 \end{bmatrix},$$

$$D_{yQ_y} = [0],$$

$$K_{yQ_y} = \begin{bmatrix} 1.12e12 & 2.47e14 & -6.19e12 \end{bmatrix}^T. \tag{A11}$$

The controllability of G_{yQ_x} is as:

$$Co_{yQ_x} = 1\times10^{-6} \begin{bmatrix} 0.0002 & -0.0002 & 0 \\ -0.2653 & 0.1493 & -0.0647 \\ -0.4522 & 0.2321 & -0.1202 \end{bmatrix}. \tag{A12}$$

BIOGRAPHIES

Moharam Habibnejad Korayem was born in Iran in 1961. He received his B.S. (Hon) and M.S. degrees in Mechanical Engineering from Amirkabir University of Technology in 1985 and 1987, respectively. He obtained his Ph.D. degree in Mechanical Engineering from the University of Wollongong, Australia, in 1994. He is currently Professor of Mechanical Engineering at the Iran University of Science and Technology, where he has been involved in teaching and research activities in the area of robotics for the last 15 years. His research interests include: Dynamics of Elastic Mechanical Manipulators, Trajectory Optimization, Symbolic Modeling, Robotic Multimedia Software, Mobile Robots, Industrial Robotics Standard, Robot Vision, Soccer Robot, and the Analysis of Mechanical Manipulator with Maximum Load Carrying Capacity. He has published more than 300 papers in international journals and at conferences in the field of robotics.

Sadegh Sadeghzadeh was born in 1983. He received his B.S. and M.S. degrees in Mechanical Engineering from Semnan University and Iran University of Science and Technology (IUST) in 2006 and 2008, respectively. He is presently a Ph.D. candidate of Mechanical Engineering at IUST. Although his current research is focused on Micro and Nano Manipulation, his research interests include: Vibration Control, Robotic and Micro and Nano Manipulation.